Aerospace Science and Technology ••• (••••) ••••••

Contents lists available at ScienceDirect

Aerospace Science and Technology

journal homepage: www.elsevier.com/locate/aescte

Numerical simulation of transpiration cooling for a high-speed boundary layer undergoing transition to turbulence

Pushpender K. Sharma [a,*], Ralf Deiterding [a], Adriano Cerminara [b], Neil Sandham [a]

[a] Aerodynamics and Flight Mechanics Research Group, University of Southampton, Boldrewood Innovation Campus, Burgess Road, Southampton, SO16 7QF, Hampshire, United Kingdom
[b] Department of Engineering and Mathematics, Sheffield Hallam University, Pond Street, Sheffield, S1 1WB, South Yorkshire, United Kingdom

ARTICLE INFO

Article history:
Received 22 May 2023
Received in revised form 3 August 2023
Accepted 14 August 2023
Available online xxxx
Communicated by Cummings Russell

Keywords:
High speed flows
Transpiration cooling
Porous layer
Transition to turbulence

ABSTRACT

Cooling the surface of high-speed vehicles by injection of coolant into the flow stream aims to reduce the overall weight and cost of thermal protection systems. Here, the transpiration-based cooling method is studied for a Mach number $M_\infty = 5$ with coolant injected through a porous layer composed of a staggered arrangement of spheres. Disturbances are introduced into the boundary layer upstream of the porous layer to study in detail the flow regime in which the boundary layer is transitional, including cases where transition is triggered either downstream or directly over the sample. The present work evaluates the effects of transition location, Reynolds number at injection location, and blowing ratio on the cooling performance downstream of the porous sample with heat fluxes that are comparable in magnitude to those seen in laboratory experiments. Flow within the porous layer is found to be unsteady, with a non-negligible streamwise pressure gradient introduced by shock and expansion waves at the leading and trailing edge of the porous sample. For cases where transition occurs just downstream of the sample, the lowest pressure/blowing ratio case results in more cooling immediately after the porous layer, but cooling performance worsens farther downstream. Higher blowing ratio cases show higher effectiveness for a longer distance downstream, despite the transition location moving upstream. For cases where transition occurs over the porous sample, the cooling effect is more consistent, with the heat flux decreasing monotonically with increasing pressure/blowing ratio. The results not only show a strong dependence on transition location, but also that opposite trends in cooling performance are possible when transition occurs just downstream of the injection.

1. Introduction

Hypersonic flight conditions can create very high values of surface temperatures and wall heat-fluxes at the vehicle surface, which can affect the structural integrity of the vehicle. This necessitates the use of a thermal protection system (TPS) to protect the interior of the vehicle. The TPS can be classified into three categories: 1) passive (such as heat sink, hot structure or insulated structure), 2) semi-passive (heat pipes and ablation), and 3) active (transpiration cooling, film cooling and convective cooling) [1]. The selection of the TPS depends upon factors such as geometry, amount of heat load and exposure time. The present study is concerned with transpiration cooling, which has attracted renewed interest for high-speed applications due to advancements in porous materials [1–3]. The method can help meet both the wall-temperature and re-usability requirements for hypersonic vehicles in very severe environments, reducing both the thickness and weight of the TPS. Therefore, it could be employed in applications with very high surface temperatures $\geq 1600\,^{\circ}\mathrm{C}$ and for flight times greater than 1.5 hours [4].

Transpiration cooling is closely related to the methods of film and effusion cooling, whereby a thin film of coolant is created on the surface of the vehicle such that the coolant absorbs the heat and changes the temperature distribution within the boundary layer [5–8]. The coolant could be liquid or gas, and it may either be inert or chemically active. The coolant injection is generally achieved by forcing the coolant through a single or multitude of holes or slots, and the coolant generally emerges as either a single sheet or a large number of individual jets. The film created by the coolant can reduce the operational surface temperature and hence either increase the external gas temperatures that the existing material can withstand, or allow a lighter/less expensive material for the structure. One prominent application of such a method is in cooling the turbine blades in jet engines. The coolant

* Corresponding author.
E-mail address: p.k.sharma@soton.ac.uk (P.K. Sharma).

https://doi.org/10.1016/j.ast.2023.108581

jets that emerge should ideally form a film close to the surface and should not cause localised boundary layer separation and transition. Therefore, it is important to manage the blowing ratio, density ratio, momentum ratio, turbulence, and other fluid conditions at the hole or slot exit to achieve optimal performance [9]. A numerical effusion cooling study, especially at high Mach number ($M_\infty = 5$) with multiple rows of slots, was performed by Cerminara et al. [10] and the results were compared against the results obtained from the experimental studies at Oxford Thermofluids Institute (OTI) [11]. It was noted that three-dimensional (3D) boundary layer instability modes with moderate disturbance amplitudes produced results which were more consistent with experimental results in terms of wall heat flux and cooling effectiveness compared to 2D instability modes.

In the method of transpiration cooling, the coolant is gently released into the flow through a porous material instead of through holes or slots used in film cooling [12–14]. This provides distributed cooling over a large surface area over and downstream of the porous layer, and also reduces the consumption of the coolant compared to film cooling. For example, in a $M_\infty = 5$ numerical flow study, Cerminara et al. [15] showed that for the same fixed mass efflux or blowing ratio, the transpiration cooling (using a porous layer composed of spheres) gave better cooling performance downstream of the injection location than effusion cooling (using multi-slot injection). In the present contribution, the transpiration cooling methodology from [15] is employed to simulate a wide range of coolant blowing ratios for two different injection locations, enabling the transpiration cooling performance to be assessed in relation to the transition location, along with developing more detailed insights into the associated flow phenomena. The numerical setup mimics the experimental setup of [14] and is set up in such a way that similar blowing ratios and comparable wall heat fluxes are obtained, as seen in the experiments.

The issue with film or effusion cooling is the impulsive injection of the coolant as jets, which can trigger early transition and change the aerodynamic performance of the lift-generating bodies, such as turbine blades, etc. For this reason, injection through two-dimensional (2D) slots is preferred over 3D slots as they help reduce the transition effects [16–18], additionally making the jets as parallel to cross-flow as possible. With transpiration cooling, on the other hand, the porous materials reduce the possibility of jet injection into the flow, preventing early transition due to the impinging jet into the high speed cross-flow as well as providing a more uniform injection of the coolant over a large surface area. However, even for transpiration cooling, very high blowing ratios could also lead to early transition, as shown in [19], which also showed that the effectiveness of transpiration cooling is much lower for turbulent flows compared to laminar flows.

Direct numerical simulation (DNS) is a useful tool for undertaking such studies, especially as it can capture small-scale flow details, which are otherwise difficult to measure experimentally. There have been very few DNS studies for transpiration cooling in the past, especially with hypersonic flow velocities and also where the results from experimental set-ups were available. Also, there are very few studies with a very long domain, considering the spatially developing boundary layer in the streamwise direction, without using a periodic boundary condition in the streamwise direction. DNS studies by [17,18] are performed only at supersonic speeds. Keller & Kloker [17] performed DNS of effusion cooling using multiple rows of discrete holes into a laminar supersonic boundary layer, while in another study, they considered the effects of foreign-gas injection into a laminar and turbulent supersonic boundary [18]. In a recent DNS study, Christopher et al. [20] presented results for transpiration cooling of a turbulent boundary layer at $M_\infty = 0.3$. The cooling was achieved through the combined effects of two mechanisms: 1) heat advection due to the non-zero wall-normal velocity at the wall, and 2) the reduction of average boundary-layer temperature due to the accumulation of coolant. The blowing was implemented through multiple small strips, and it was shown that when the strips are made incrementally smaller, the results match with uniform blowing over the entire surface.

The present study also looks into the transition to turbulent aspects but at hypersonic speeds, where very few detailed DNS studies are available for transpiration cooling. There have been some studies using Reynolds Averaged Navier-Stokes (RANS) modelling [21,22], but such studies require tuning of the modelling coefficients. DNS studies could be very helpful for RANS as these provide very detailed statistics of the flow. The configuration, simulated here, is taken from experiments performed by [14]. Section 2 provides the details of the governing equations used and the details of the flow solver along with the numerical methods utilised. The details of the numerical set-up used are presented in Section 3, giving details about domain initialization and boundary conditions, etc. Instead of using an isothermal wall, a simple conjugate heat-flux (CHF) model is employed at the wall to evaluate the surface temperature based on the equivalence of heat flux from the fluid and solid sides. The validation for the same is presented in Section 3. Section 4 presents the results from various cases, with and without coolant injection, for the two different porous layer placement locations. Section 5 provides the concluding remarks about the paper.

2. Governing equations and numerical methods

2.1. Governing equations

The system of 3D non-dimensional governing fluid mechanical equations is solved in the conservative form for the compressible multi-species flow and is presented in the Cartesian coordinate system as follows,

$$\frac{\partial \rho}{\partial t} + \frac{\partial \rho u_j}{\partial x_j} = 0, \tag{1}$$

$$\frac{\partial \rho u_i}{\partial t} + \frac{\partial \rho u_i u_j}{\partial x_j} = -\frac{\partial p}{\partial x_i} + \frac{1}{Re_{\delta_1^*}} \frac{\partial \tau_{ij}}{\partial x_j}, \tag{2}$$

$$\frac{\partial \rho E}{\partial t} + \frac{\partial \left(\rho E + p\right) u_j}{\partial x_j} = \frac{\partial}{\partial x_j}\left(\kappa \frac{\partial T}{\partial x_j}\right) + \frac{1}{Re_{\delta_1^*}} \frac{\partial \tau_{ij} u_i}{\partial x_j}, \tag{3}$$

$$\frac{\partial \rho Y_1}{\partial t} + \frac{\partial}{\partial x_j}\left(\rho Y_1 u_j - \rho D \frac{\partial Y_1}{\partial x_j}\right) = 0. \tag{4}$$

Equations (1) to (4) show the non-dimensional form of mass conservation equation, three momentum conservation equations, the energy conservation equation, and the species conservation equation for a single coolant, respectively. The indices i and j run from 1 to 3. It is important to note that these equations are written under the assumption of constant specific heats as low temperature ($T^*_\infty = 76.66$ K) hypersonic flow ($M_\infty = 5$) is studied, and activation of vibrational modes and dissociation of molecules is negligible, and hence ignored. In the equations, $\rho = \rho^*/\rho^*_\infty$ is the non-dimensional density, $u_1 = u = u^*/U^*_\infty$, $u_2 = v = v^*/U^*_\infty$ and $u_3 = w = w^*/U^*_\infty$ are the non-dimensional velocity components respectively in the x-, y- and z-directions scaled with free-stream velocity (U^*_∞). $E = e + 1/2\rho(u^2 + v^2 + w^2)$ is the total energy per unit mass (with e as specific internal energy), and Y_1 is the mass fraction of the coolant. The terms ρ, ρu, ρv, ρw, ρE, and ρY_1 are the corresponding conservative variables. The terms p, T are the non-dimensional pressure and temperature, respectively, while $\tau_{ij} = \mu\left[\partial u_i/\partial x_j + \partial u_j/\partial x_i - 2/3(\partial u_k/\partial x_k)\delta_{ij}\right]$ is the viscous stress tensor, where μ is the non-dimensional dynamic viscosity and δ_{ij}

is the Kronecker delta function. The various physical variables are normalised using the corresponding free-stream values. However, pressure is normalised using the free-stream dynamic pressure term, $\rho^*_\infty U^{*2}_\infty$, i.e., $p = p^*/\rho^*_\infty U^{*2}_\infty$, while the unit total energy, E is normalised by U^{*2}_∞. The dimensional quantities are denoted by a superscript $(^*)$, and it is dropped for non-dimensional quantities until mentioned otherwise. Also, the subscript $(_\infty)$ represents the free-stream conditions at the inflow. $x = x^*/\delta^*_1$, $y = y^*/\delta^*_1$ and $z = z^*/\delta^*_1$ are the non-dimensional coordinates scaled with the displacement thickness $\delta^*_1 = 1$ mm at the inflow. The characteristic fluid dynamic time scale is δ^*_1/U^*_∞.

The transport properties corresponding to mass, momentum, and thermal diffusion are D, μ, and κ, respectively, and are a function of temperature. As the single species coolant that is used in the present study is cold air, the air-to-air binary mixture's dynamic viscosity and thermal conductivity remain the same as that of the air and are found in [23,17,24]. The simplified expressions for dynamic viscosity (Eq. (5)), thermal conductivity (Eq. (6)), and mass diffusivity (Eq. (7)) in the non-dimensional form are presented below for clarity,

$$\mu = \mu^*/\mu^*_\infty = (T^*/T^*_\infty)^{3/2}\frac{(T^*_\infty + S^*)}{(T^* + S^*)} = (T)^{3/2}\frac{(1 + S^*/T^*_\infty)}{(T + S^*/T^*_\infty)}, \tag{5}$$

$$\kappa = \frac{\mu}{(\gamma - 1)Re_{\delta^*_1} PrM^2_\infty}, \tag{6}$$

$$D = \frac{\mu}{\rho Re_{\delta^*_1} Sc}, \tag{7}$$

Here, $S^* = 110.4$ K is the Sutherland constant, $Re_{\delta^*_1} = 12600$ is the simulations Reynolds number, $M_\infty = 5$ is the free-stream Mach number, and Pr is the Prandtl number. γ is the ratio of specific heats of air in the freestream ($\gamma = c^*_{p,\infty}/c^*_{v,\infty} = 1.4$). Also, the specific heats of the air-to-air mixture, i.e., c_p and c_v, are constant and are the same as that of air, implying a constant $\gamma = 1.4$ in the simulations. The boundary-layer displacement thickness (δ^*_1) at the inflow plane is used as the characteristic length scale, and the simulation Reynolds number defined based on it is $Re_{\delta^*_1} = (\rho^*_\infty U^*_\infty \delta^*_1)/\mu^*_\infty$. A fixed Prandtl number of $Pr = 0.72$ is used in the simulations. In Eq. (7), $Sc = \mu^*/(\rho^* D^*)$ is the Schmidt number which is set as $Sc = 1$ for the present case of air-to-air injection into a turbulent boundary layer; hence the expression for D simplifies to $D = \mu/\rho Re_{\delta^*_1}$.

The temperature T is evaluated from the energy definition

$$E = \frac{1}{\gamma M^2_\infty} c_v T + \frac{1}{2}\left(u^2 + v^2 + w^2\right). \tag{8}$$

Once the temperature is evaluated, the non-dimensional form of the equation of state is used to calculate the pressure p, in terms of T and the density ρ as

$$p = \frac{1}{\gamma M^2_\infty}\rho RT \tag{9}$$

Here, the non-dimensional gas constant of the mixture in general is $R = R^*/R^*_\infty$, where $R^*_\infty = 287.058$ J/(Kg K). Since an air-air binary mixture is considered where the free-stream fluid is air and the coolant considered is also air at a low temperature, the specific heats of the mixture are the same. Hence, the mixture non-dimensional gas constant becomes unity, i.e., $R = R^*/R^*_\infty = 1$, and Eq. (9) simplifies to $p = (1/\gamma M^2_\infty)\rho T$.

2.2. Numerical methods

The solver used is an in-house solver called AMROC (Adaptive Mesh Refinement using Object-Oriented C++) [25]. It is a finite-volume-based solver and provides structured adaptive mesh refinement (SAMR) capability. The SAMR allows for higher resolution in the small length scale of the porous layer in the present case, while it is also, in general, helpful to provide multiple mesh refinement levels in the regions of the flow with high gradients where the levels are added in a patch-wise manner; see [25]. This capability not only helps in reducing the computational cost but also helps in increasing the numerical stability and accuracy of the solution.

A hybrid WENO-CD scheme is used, i.e., 6^{th}-order central differencing (CD) scheme in space for both inviscid and viscous fluxes, combined with a 6^{th}-order weighted-essentially-non-oscillatory (WENO) scheme for shock-capturing, and has been tested and validated for multiple compressible flow problems in the past [26–29,15]. A 3^{rd}-order Runge-Kutta method is used for time integration.

A switch is used in the hybrid WENO-CD scheme to switch from the central scheme in the smooth regions to the WENO scheme in regions of sharp gradients/ discontinuities. The technique is based on an approximate Riemann solver to detect the presence of strong shock waves, while the weak ones are ignored. The Roe-averaged quantities are used to find the approximate solution to the Riemann problem at cell interfaces, from the respective given left (L) and right (R) states. The waves (shock or rarefaction) are distinguished based on Liu's entropy condition, which utilises the characteristic speeds associated with the eigenvalues $u \pm a$. The strict condition for the generation of a shock is

$$|u_L \pm a_L| \geq |u_* \pm a_*| \geq |u_R \pm a_R|, \tag{10}$$

where a_L and a_R are the sound speeds evaluated at the left and right cell interfaces, while $*$ quantities, corresponding to the central state, are evaluated using Roe averages. Weak acoustic waves, which are easily handled by central schemes, can be eliminated by employing a threshold value for the inequalities in Eq. (10), i.e., the difference between the characteristics based on the left and right states has to be bigger than a certain imposed threshold (th_1) decided by the user. Once the previous condition is satisfied at a cell interface between cells at j and $j+1$, for achieving efficiency and flexibility, an additional smoothness test is used based on the normalised pressure gradient ($\theta_j = |p_{j+1} - p_j|/|p_{j+1} + p_j|$) using the function

$$\phi(\theta_j) = 2\theta_j/(1 + \theta_j)^2. \tag{11}$$

If $\phi(\theta_j) > \theta_2$ across a cell interface, where θ_2 is a user-decided threshold value to additionally identify high pressure gradient in the regions identified by Eq. (10), the particular cell interface is flagged to use the WENO method for flux evaluation.

3. Numerical set-up

The numerical set-up used in the present simulations mimics the experiments performed in the high-density tunnel at OTI by Hermann et al. [14], using Ultra-High Temperature Ceramic (UHTC) as the porous material. A 2D schematic of the whole configuration is shown in Fig. 1. The porous layer, marked as UHTC, is placed at x^*_{inj} from the inflow plane of the computational domain or equivalently at $\tilde{x}^*_{inj}$ from the leading edge of the flat plate. The inflow plane of the computational domain is at $\tilde{x}^*_0 \approx 127$ mm from the leading edge. Note that the x with and without tilde is the

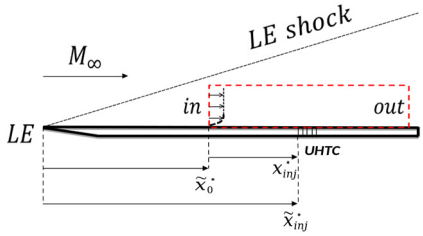

Fig. 1. Schematic of the full configuration, with the computational domain marked by the red dashed line. (For interpretation of the colours in the figure(s), the reader is referred to the web version of this article.)

Table 1
Free-stream conditions.

M_∞	Re_u (1/m)	T_∞^* (K)	ρ_∞^* (Kg/m^3)	p_∞^* (Pa)
5	12.6×10^6	76.66	0.07979	1.75×10^3

distance measured from the leading edge and the computational inflow plane, respectively. The free-stream conditions are tabulated in Table 1, which correspond to an inflow Mach number of $M_\infty = 5$, and free-stream temperature of $T_\infty^* = 76.66$ K. These conditions result in a unit Reynolds number of $Re_u = \rho_\infty^* U_\infty^* / \mu_\infty^* = 12.6 \times 10^6$ (1/m) and a boundary layer displacement thickness of $\delta_1^* = 1$ mm at the computational inflow plane.

The computation domain is a 3D rectangular box with periodicity in the spanwise (z-direction). The computational domain is marked by the red dashed line in the schematic Fig. 1. A 2D schematic in Fig. 2 shows the basic idea of transpiration cooling, where the coolant, while passing through the porous layer, cools it and then cools the oncoming hypersonic external flow. The coolant in Fig. 2 is shown to be injected through a 2D porous layer composed of three rows of staggered cylinders in 2D. However, in the 3D simulations, the artificial porous layer is created using three rows of staggered spheres (in a body-centred cubic packing). The extents of the domain in x, y, and z directions are 0 to 160, -1.28 to 22.72, and -4 to 4, respectively. A grid/mesh with $N_x \times N_y \times N_z = 2000 \times 300 \times 100$ cells is used for the coarsest level. Two levels of refinement are used for these cases. It takes about 48,000 CPU-hours to reach the non-dimensional time $t = t^*/(\delta_1^*/U_\infty^*) \approx 500$, (or dimensional time $t^* = 0.569$ ms) using 400 processor cores.

As mentioned earlier, the solver is an adaptive mesh refinement solver, and for the current simulations, two levels of meshes are used, i.e., a coarsest base mesh and a second level mesh with a refinement factor of two inside the porous layer and very close to the flat plate wall. This is depicted in Fig. 3, with the figure in the inset showing a magnified view of the grid near the leading edge of the porous layer. The refinement factor is the factor by which the previous level grid spacing is divided to obtain the successive level grid spacing. An early grid study was carried out using a two-level mesh with increasing refinement factors of 2, 3 and 4 for one of the blowing cases. This resulted in percentage differences in the mean blowing ratio of 2.5% for a refinement factor of 2 and 1.0% for a refinement factor of 3, compared to the most refined grid with a refinement factor of 4, with no substantial changes in flow structure. The refinement factor of 2 was subsequently used for all the simulations. Further details on grid spacings and wall units justifying the use of the present grid are presented in Section 4.3.

A porous layer of dimensions 39 mm × 39 mm is used in the experimental study of Hermann et al. [14]. However, as the porous layer is considered to be uniform in the spanwise direction, to save computational costs, only an 8 mm wide porous layer is considered in the numerical simulations. This effectively provides the same amount of mass efflux through the numerical porous layer as would be found in the experiments, provided a similar blowing ratio (i.e., the ratio of normal coolant mass flux to the free-stream mass flux) is maintained over the porous layer. Therefore, the space-time averaged blowing ratios in the numerical simulations are matched to those reported in the experiments. As higher pore sizes are used in the mesoscopic model of the porous layer, smaller values of pressure ratios (PR) are required to obtain similar blowing ratios as reported in the experiments. The position of the leading edge of the porous layer determines the Reynolds number at the injection location, i.e., Re_{inj}. Here, two particular injection Reynolds numbers, i.e., $Re_{inj,1} = 2.04 \times 10^6$ and $Re_{inj,2} = 2.18 \times 10^6$ are considered, both of which show high surface heat fluxes in experiments without coolant injection [14].

3.1. Boundary conditions

Inflow conditions correspond to the free-stream conditions present in the experiment and are tabulated in Table 1. The non-dimensional values of density, temperature, and pressure are $\rho_\infty = 1$, $T_\infty = 1$, and $P_\infty = 1/(\gamma M_\infty^2) = 0.02857$. The inflow boundary layer profiles corresponding to these inflow conditions are imposed at the inflow boundary as described in detail in subsection 3.2. Supersonic outflow boundary conditions are applied at the outflow of the computational domain, where variables are extrapolated from inside the domain. Far-field boundary conditions are used at the top boundary, assuming zero gradients of the conservative variables. Periodic boundary conditions are used in the spanwise direction. The bottom flat plate at $y = 0$ is a no-slip wall with disturbances introduced in the v-component of velocity, as detailed in subsection 3.2. Additionally, a conjugate heat-flux (CHF) wall boundary condition is applied for the evaluation of the wall temperature. This is done by assuming a solid material of a certain thickness underneath the wall at $y = 0$. The material is chosen as aluminium with thermal conductivity of $\kappa^* = 237$ W/m^2 and thickness of 20 mm with the bottom of the solid maintained at $T_{solid}^* = 290$ K. The spheres in the porous layer are represented as embedded boundaries [30] with no-slip on the spherical surfaces and are maintained at a constant temperature as the coolant surrounding these, i.e., at $T_c^* = 290$ K. Also, the bottom of the plenum chamber continuously supplies the coolant at a constant temperature of $T_c^* = 290$ K. An initial comparison was performed with the isothermal wall boundary conditions and only a marginal difference was noted between the results.

Validation of the CHF wall boundary condition was performed using a flat plate with a sharp leading edge included in the computational domain. All parameters in this validation part are in dimensional form; hence, the superscript * is dropped from all terms for simplicity. Again, the same material of aluminium is considered with a thickness of 1 m. The temperature at the interface of the solid and the fluid is evaluated using the heat flux equivalence condition, i.e., equating the conductive heat flux from the solid side to the fluid side, which is mathematically written as follows:

$$\kappa_g \frac{\partial T^+}{\partial y} = \kappa_s \frac{\partial T^-}{\partial y}, \tag{12}$$

where κ_g and κ_s are the thermal conductivity of the gas and solid, respectively. Also, $\partial T^+/\partial y$ and $\partial T^-/\partial y$ represent the gradient of temperature evaluated at $y = 0$ in the fluid side (in positive y-direction) and solid side (in negative y-direction), respectively. Here, steady-state heat conduction is assumed inside the solid, and hence a linear temperature profile is assumed inside the solid thickness. The thermal conductivity of the gas is evaluated as $\kappa_g = \mu c_p / Pr$. Once the temperature at the bottom of the solid (T_{solid}) is fixed, the interface or wall temperature (T_{wall}) is evaluated using the equivalence condition of Eq. (12).

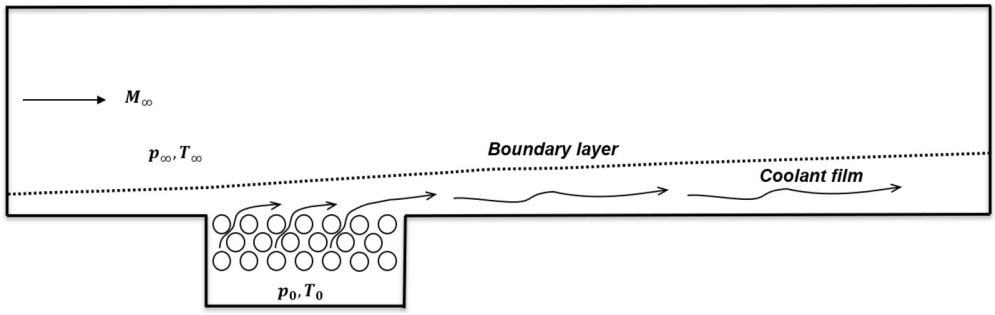

Fig. 2. Schematic of the porous layer in relation to the boundary layer.

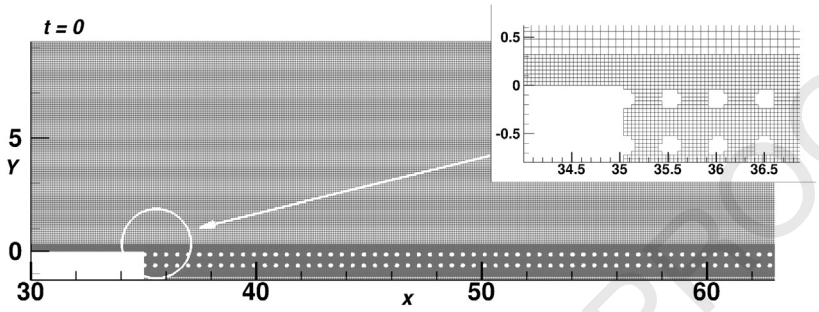

Fig. 3. Two levels of mesh are shown at $t = 0$ at an x-y plane at $z = -0.001$ plane and a magnified view near the porous layer leading edge is shown in the inset. The 2D cut section of the 3D porous layer only captures the top and bottom rows of spheres, and doesn't show the third intermediate layer of spheres in the figure.

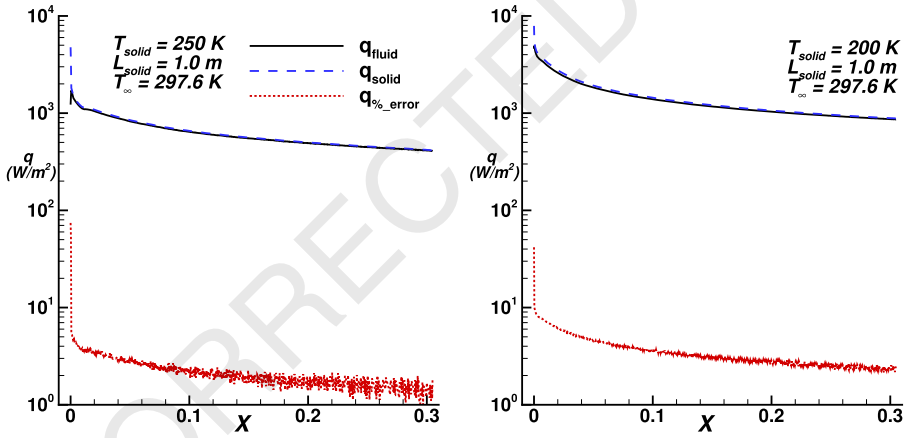

Fig. 4. Comparison of heat fluxes from the fluid and solid sides for two different solid bottom temperatures, where the left and the right frames show $T_{solid} = 250$ K and 200 K, respectively. An ambient temperature of $T_\infty = 297.6$ K is used in both cases. The vertical axis is in log scale, and the % error is also plotted, showing the differences between the fluxes from the two sides.

Fig. 4 shows the streamwise variation of the wall heat fluxes evaluated using the CHF boundary condition of Eq. (12). In the figure, heat fluxes at the wall, evaluated from the fluid and solid sides, are represented as q_{fluid} and q_{solid}, respectively. Since q_{fluid} and q_{solid} should be equal, a difference between the two is plotted as the percentage error as $q_{\%\_\text{error}} = |q_{\text{fluid}} - q_{\text{solid}}|/q_{\text{solid}} \times 100$. Two cases are presented. The left frame shows the cases where the bottom of one meter thick solid is fixed at $T_{\text{solid}} = 250$ K, while in the right frame, it is fixed at $T_{\text{solid}} = 200$ K. The frame on the right shows higher wall heat flux values than on the left due to the higher temperature gradient between the solid and the free-stream temperature, which is kept constant at $T_\infty = 297.6$ K in both cases. It can be seen from Fig. 4 that the CHF boundary condition works well, and the % error between the heat fluxes evaluated at the interface is small (1 to 3%), except close to the leading edge where the leading edge effects cause a massive increase in the heat flux values. This happens because the leading edge is sharp and hence results in a significant adjustment of the parallel oncoming free-stream flow. The error downstream, however, is primarily due to the use of a relatively coarser grid and the use of first-order differences for heat flux evaluation.

3.2. Initialization

The computational inflow plane is chosen in such a way that the displacement thickness (δ_1^*) for the imposed unit Reynolds number ($Re_u = 12.6 \times 10^6$ (1/m)) is 1 mm at the inflow plane. This distance is approximately 127 mm from the leading edge of the flat plate, i.e., $\tilde{x}^* \approx 127$ mm. This $\delta_1^* = 1$ mm is also used as the length scale for scaling the distances in the present computations, and therefore, the imposed Reynolds number in the simulations is $Re_{\delta_1^*} = \rho_\infty^* U_\infty^* \delta_1^* / \mu_\infty^* = 12600$. For the given unit Reynolds number of $Re_u = 12.6 \times 10^6$ (1/m), two particular Re_{inj}, i.e., $Re_{inj,1}$ and $Re_{inj,2}$ are obtained corresponding to the leading edge of porous

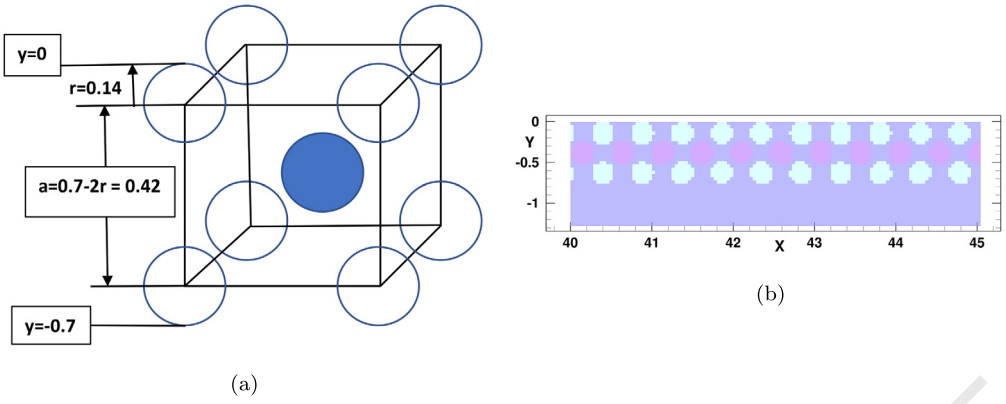

Fig. 5. (a) shows the sphere packing arrangement for a unit cell. (b) shows two z-planes (with 50% translucency) in a smaller domain within the porous layer such that the maximum extent of the spheres in the outer layers (cyan) and staggered central layer (blue) is captured.

layer placed at $x = 35$ and $x = 46$ from the computational inflow plane, respectively, or $\tilde{x} = 127 + 35 = 162$ and $\tilde{x} = 127 + 46 = 173$ from the flat plate leading edge, respectively.

The spheres of the porous sample are packed in a body-centred cubic (BCC) arrangement in which the spheres do not touch each other. The sphere arrangement is selected based on a previous study by Cerminara et al. [15], where it was demonstrated that equivalent flow behaviour at different pore scales could be obtained with sphere arrangement. The model was validated against Lee and Yang's [31] computational model, which was also further compared against the empirical model of Ergun [32] based on experimental results for granular porous media. There are three layers of the spheres forming a porous layer of thickness 0.7 mm (along y-axis between $y = 0$ and $y = -0.7$), width 8 mm (along z-axis between $z = -4$ and $z = 4$), and length 39 mm (two configurations along x-axis between (a) $x = 35$ and $x = 74$, and (b) $x = 46$ and $z = 85$). A plenum chamber below the porous layer between $-1.28 \leq y \leq -0.7$ is created to hold the coolant at higher pressure. The non-dimensional radius of the spheres in the present arrangement is $r = 0.14$.

Fig. 5a shows the arrangement of spheres for a unit cell in the matrix. As the top and bottom of the sphere layer are between $y = 0$ and $y = -0.7$, the side of the cube is $a = 0.7 - 2r = 0.42$. The porosity of this structure is defined as ϵ and is the ratio of void volume to the total volume of the cell. This can be written mathematically as $\epsilon = [a^3 - 2(\frac{4}{3}\pi r^3)]/a^3$ or $\epsilon = 1 - \frac{8}{3}\pi(r/a)^3$. So, porosity for $r = 0.14$ and $a = 0.42$ is approximately 0.689 or 68.9%. Fig. 5b shows the staggered arrangement by plotting two different spanwise planes with 50% translucency such that the maximum extent of the spheres in the outer two layers is captured along with the staggered central layer of the spheres.

The local blowing ratio is the ratio of the vertical mass flux of the coolant at the exit of the porous layer (at $y = 0$) scaled with the free-stream mass flux and is defined as $F = (\rho^* v^*)_{injection}/(\rho^* U^*)_\infty = (\rho v)_{injection}$, where $\rho = \rho^*/\rho^*_\infty$ and $v = v^*/U^*_\infty$ are the non-dimensional density and wall-normal component of velocity, respectively, at the injection location. For the *no-blowing* cases, a pressure ratio (PR) of one is maintained through the porous layer, i.e., $PR = P_{plenum}/P_\infty = 1$, resulting only in negligible blowing ratios (as seen in Figs. 11 and 21), whereas for the blowing cases, a value of PR greater than one is chosen which results in a significantly higher blowing ratios. For the blowing cases, the pressure is initialised as constant in the plenum chamber ($-1.28 \leq y \leq -0.7$) at $P_{plenum} = PR \times P_\infty$, with a linear pressure distribution inside the porous layer thickness, reaching the free-stream pressure value at the exit of the porous layer. A constant coolant temperature, $T^*_c = 290$ K, and coolant concentration of unity ($Y_1 = 1$) are imposed inside the plenum chamber and porous layer.

It is noted that the flow in the experiments is transitional and results in higher wall heat flux values than for laminar flow. Keeping this in mind, in the numerical simulations, time-harmonic streamwise and spanwise modulated disturbances are imposed in the v-component of velocity ahead of the porous layer between $x = 10$ and $x = 30$. The disturbances are partly derived from a previous study based on linear stability theory (LST) shown in [10], where three modes in the spanwise direction were used. In the present simulations, a non-dimensional disturbance function is defined by

$$v'(x, z, t) = A \cos(\beta_0 z) \cos[\alpha_0 (x - x_0) - \omega_0 t] \ , \qquad (13)$$

where A is the amplitude of the imposed disturbances, $\beta_0 = 2\pi/\lambda_z \approx 0.2387$ is the spanwise wavenumber corresponding to the non-dimensional spanwise wavelength of 8/3, i.e., $\lambda_z = 8/3 = 2.67$ assuming three sinusoidal spanwise waves in the entire spanwise length of the domain, and $\alpha_0 = 2\pi/\lambda_x \approx 0.314$ is the streamwise wavenumber for the non-dimensional streamwise wavelength of $\lambda_x = (30\text{-}10) = 20$. Also, $x_0 = 10$ and a non-dimensional frequency of $\omega_0 = 0.162$ are used, with a non-dimensional time period of $t_0 = 38.8$, which allows the disturbances to convect downstream with time. These time-harmonic blowing-suction disturbances are introduced at the wall in the v-component such that mass conservation is not violated at any given time. A single spanwise mode of disturbances is chosen such that the coolant downstream is mixed in a uniform manner.

The amplitude of disturbances is chosen by performing a few initial computations to get results comparable to the experiments, bearing in mind the significant error bars on the measurements. Table 2 shows a comparison of heat fluxes from various no-blowing cases. The heat fluxes are measured at the same distance downstream of the porous sample as in the experiments approximately 43 mm downstream of the porous sample. This translates to $x = 117$ and $x = 128$, for $Re_{inj,1}$ and $Re_{inj,2}$ cases, respectively, in the computational domain. It is apparent from the table that heat flux is mainly sensitive to the disturbance amplitude, with a secondary effect being the streamwise location of the placement of the porous sample. Nevertheless, slightly higher heat fluxes are observed for the downstream injection location ($Re_{inj,2}$) compared to the upstream injection location ($Re_{inj,1}$) for similar amplitudes. It is also important to note to achieve similar levels of heat flux values as noted in the experiments, higher levels of disturbance amplitudes (A=5% and 10%) were required (the values of heat fluxes observed for the laminar cases without any perturbations are too low to start with). This is due to the fact that the domain used in

Table 2
Wall heat flux comparison with experiments.

Case	Amplitude (%)	Simulation wall heat flux values (kW/m^2)	Simulation exact values (kW/m^2) at measurement location	Experimental wall heat flux values (kW/m^2)
Laminar	0	≈ 2	1.577	NA
$Re_{inj,1}$	5	$\approx$ 5-6	5.223	5-10
	10	$\approx$ 7-8	7.400	
$Re_{inj,2}$	5	$\approx$ 5-6	5.700	10-11
	10	$\approx$ 7-8	7.650	

Table 3
Cases considered for $Re_{inj,1} = 2.04 \times 10^6$.

Case No.	PR	Disturbance Amplitude
1a	1	5%
2a	1.15	5%
3a	1.3	5%
4a	1.5	5%

the computations starts far downstream from the leading edge of the flat plate to save computational cost, whereas, in the experiments where the setup has a sharp leading edge, the instabilities get a longer stretch for growth before reaching the porous sample.

4. Results and discussion

Two configurations were chosen for the detailed coolant injection study from Table 2, corresponding to the lowest ($A = 5\%$) and highest ($A = 10\%$) heat flux cases with no-blowing for $Re_{inj,1}$ and $Re_{inj,2}$, respectively. We begin by considering the case of lower disturbance amplitude ($A = 5\%$) and upstream location ($Re_{inj,1}$), for which the various cases with/without coolant injection are listed in Table 3.

4.1. Overview of flow development and structure

The temporal development of three-dimensionality in the flowfield is illustrated for Case-2a in Fig. 6, where the coolant concentration (Y_1) contours are plotted on an x-z plane at $y = 1$, which is slightly away from the wall but still within the turbulent boundary layer during the flow development period. The streaky nature of the disturbances is apparent, with the streaks elongating and starting to show instability towards the leading front of the coolant motion as time increases. This leading front eventually breaks down and becomes turbulent with a clear transitional location at $x \approx 100$. The flow before the transition location is dominated by a few spanwise and streamwise wavenumbers, whereas for $x \geq 100$, multiple scales are generated, resulting in multiple spanwise and streamwise wavenumbers, which is generally a characteristic of turbulent flows. Here also, a more uniform mixing of coolant is noted. In the following discussion, only the fully developed flow is shown, and average quantities are computed after allowing for the initial transient to pass.

In Fig. 7, the developed ($t = 456$) coolant concentration (Y_1) contours are plotted for Case-2a on y-z planes at different x locations. At $x = 70$, the coolant fills the porous layer section completely, and large peak and valley structures are observed outside the porous layer, which arise from the imposed disturbances upstream. As one moves downstream of the porous layer, the peaks and the valleys alternate, such that peaks appear at the valley locations and vice versa when tracked along fixed spanwise locations along the streamwise direction, as one moves from $x = 70$ to $x = 80$, and then to $x = 90$. As transition occurs, the structures become more diffuse, with lower concentration close to the wall.

The present mesoscale model represents a porous surface by a regular array of spheres which may be larger than those in a material sample. It is, therefore, important to document the flow within the porous layer. This is demonstrated in Fig. 8, where the instantaneous v-component of velocity is presented on three x-z slices within the porous layer at $y \approx 0$, $y = -0.5$, and $y = -1.0$ for Case-4a. At $y \approx 0$, we see the flow emerging from the porous layer into the boundary layer. The flow has strong variation, not only in the streamwise direction but also in the spanwise direction, due to the transitional nature of the flow over the porous layer. Further down in the layer at $y = -0.5$, we see a decreased amplitude of disturbances and a more uniform blowing profile. However, as seen at $y = -1.0$, some disturbances are present below the whole porous layer. Although beyond the scope of the present study, it would be of interest in future work to run cases with many more layers of spheres to see how far disturbances propagate before being damped out and also to check the accuracy of simplified boundary conditions for linearized stability calculations.

4.2. Effect of blowing ratio

The effect of blowing ratio is first considered for the same case as in the previous subsection, i.e., where the leading edge of the 39 mm long porous layer is placed at $x = 35$, corresponding to $Re_{inj,1}$ as presented in Table 3. Case-1a represents the *no-blowing* case with $PR = 1$ across the porous layer, resulting in a blowing ratio of zero. Case-2a, Case-3a, and Case-4a represent the case with coolant blowing with increasing PR and F. 3D views of the flow field are shown in Figs. 9 and 10 for Case-2a and Case-4a, respectively, in a subset of the domain with $50 \leq x \leq 160$, $-1.28 \leq y \leq 5$, and $-4 \leq z \leq 4$. In both the figures, the coolant concentration (Y_1) is plotted on the x-z plane at $y = 0.1$ and on various y-z planes at different streamwise locations, i.e., $x = 60$, 80, 100, 120, 140, 160. The u-component of velocity is plotted on the x-y plane at $z = -4$, which shows the corresponding development of the boundary layer. The side plane at $z = -4$ in Fig. 9 shows a highly perturbed boundary layer, with evident distortion of the boundary layer edge, up to about $x \approx 100$, and then, further downstream, it undergoes breakdown process with fragmentation and randomisation. Three distinct peaks are noted at $x = 60$ on the y-z plane which show a correlation with the imposed three-mode disturbances upstream. However, due to the transition starting at $x \approx 90$, the coolant starts mixing and becomes more distributed in the flow domain, showing higher mixing at farther downstream locations. The coolant concentration is also seen to fade away due to mixing as one moves downstream. In contrast, for the high PR Case-4a shown in Fig. 10, the boundary layer is already transitional from $x = 50$ itself, as noted from the side plane at $z = -4$, suggesting that the boundary layer becomes transitional over the porous layer itself between $35 \leq x \leq 74$. Also, the boundary layer for Case-4a is much thicker compared to Case-2a due to a higher blowing ratio. As Case-4a is the case with highest blowing ratio, the coolant concentration is much higher than Case-2a and hence, has a higher

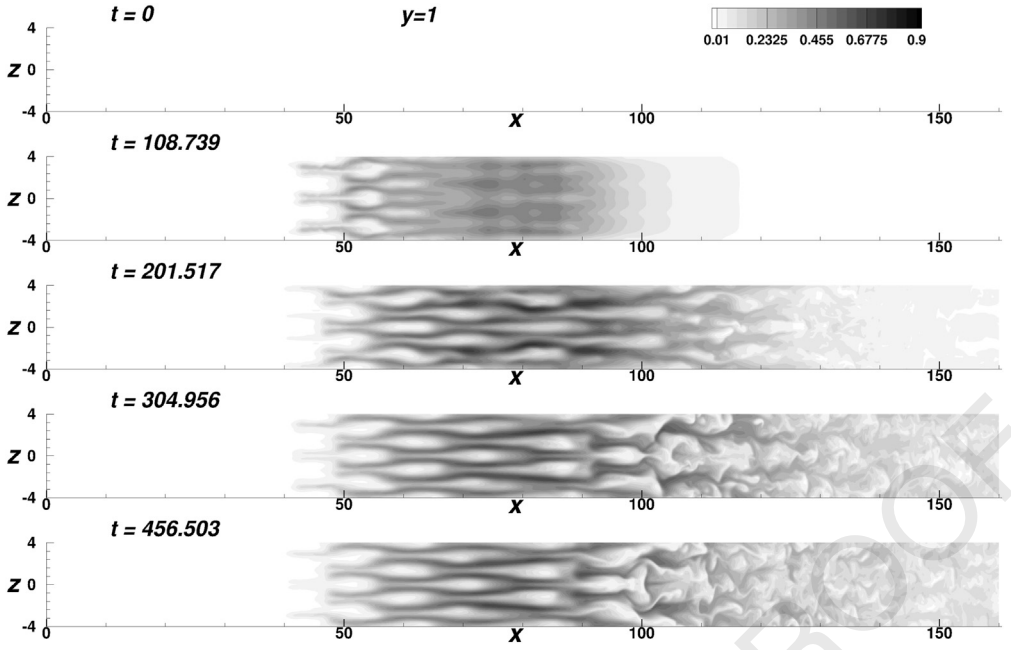

Fig. 6. Coolant movement with time (Y_1 contours) at an x-z plane at $y = 1$ for Case-2a.

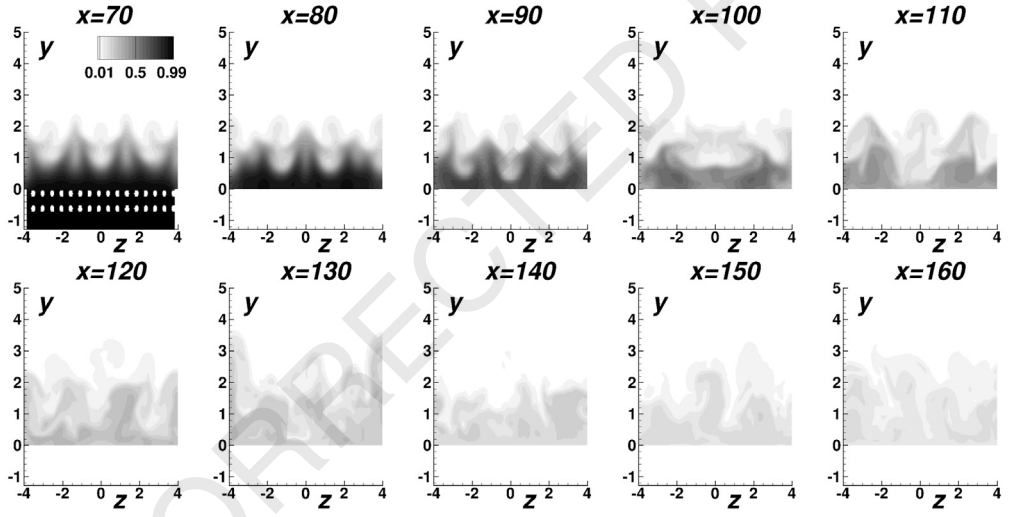

Fig. 7. Coolant distribution (Y_1 contours) at different y-z planes at $t \approx 456$ for Case-2a.

distribution in all three directions downstream of the porous layer compared to Case-2a.

The streamwise variations of the span- and time-averaged vertical blowing ratios at the exit of the porous layer for different cases of Table 3 are shown in Fig. 11. As seen from the figure, the blowing ratio is nearly zero for the no-blowing case, while the blowing ratio magnitude increases with increasing pressure ratios. The local blowing ratios decrease slightly just downstream of the porous layer leading edge, with a higher decrease being noted for the increasing PR. The largest departure from uniform blowing is seen towards the rear of the porous patch, where much larger injection velocities are observed.

To investigate this in more detail, Fig. 12 shows the normalised pressure (top frame) and streamtraces with v-component contours (bottom frame) for Case-4a on an x-y plane at $z = -0.001$. The top frame shows the weak oblique shock forming ahead of the porous layer leading edge, which increases the pressure and also deflects the flow vertically, as shown in the bottom frame with the help of streamtraces that are released from the inflow plane for $0 \leq y \leq 5$. Also, towards the trailing edge of the porous layer, the pressure starts to drop and the v-component of velocity increases, resulting in the streamtraces, released from the plenum chamber, to penetrate higher into the cross-flow. The streamtraces released from the inflow plane are also pushed slightly towards the wall, with a small negative v-component of velocity, as these pass through this expansion region. Here, a streamtrace defines the path traced by mass-less particles placed at an arbitrary location in a steady-state vector field, and constructed using the u- and v-velocity components on the particular plane, ignoring the w-velocity component.

With this detailed picture in mind, we can now confirm that the reduced blowing ratios/velocities, seen over roughly the front three-quarters of the porous sample in Figs. 8 and 11, is explained by the formation of a weak oblique shock above the porous layer due to the interaction of the ejected coolant and the hypersonic cross-stream. As the amount of coolant ejected increases with increasing PR, the porous layer leading shock becomes stronger. At the rear of the porous layer, there is an expansion caused by the external flow turning back over the injected fluid, which draws

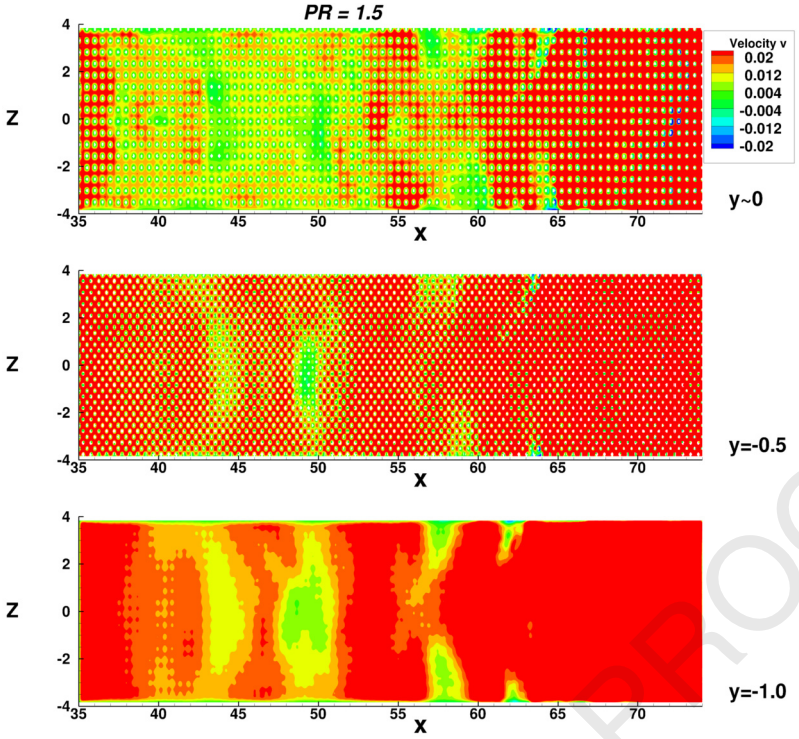

Fig. 8. Disturbance penetration into the porous layer shown using the instantaneous v-component of velocity on three x-z slices at $y \approx 0$, $y = -0.5$, and $y = -1.0$ for Case-4a.

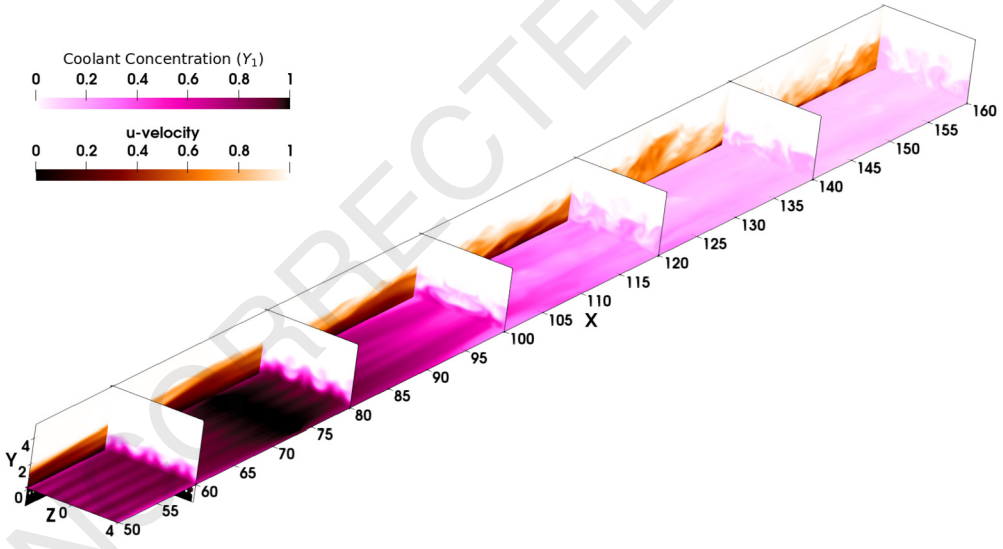

Fig. 9. 3D view of flow field for Case-2a at $t = 456.5$, showing a) coolant concentration (Y_1) on x-z plane at $y = 0.1$ and on various y-z planes along x-direction, b) u-velocity component on x-y plane at $z = -4$.

more fluid out of the porous layer, causing a large increase in the local blowing ratios/ velocities at the back of the porous sample.

For completeness, Fig. 13 shows the span-time averaged pressure at the wall. The pressure starting at the inflow plane is approximately $p_\infty = 0.02857$ and then rises to $1.5 \times p_\infty = 0.042855$ over the porous sample. The start of the pressure rise is upstream of the porous layer where the boundary layer separates. This separation and a small region of reverse flow can also be seen in the streamtraces shown in Fig. 12. The drop in pressure towards the end of the porous sample can be clearly observed, leading to the locally increased blowing ratios.

Before finding the time- and span-averaged wall heat fluxes, it is important to check when the coolant reaches the exit of the domain and achieves a statistically stationary state. To demonstrate this, Fig. 14 is plotted, which shows the evolution of streamwise variation of coolant concentration at various times and also shows the time-averaged values for the data for $t > 300$. It is observed that the coolant reaches the exit at about $t \approx 250$, and the coolant concentration oscillates about the time-averaged mean value when the averaging is done for $t > 300$. This demonstrates that the flow has reached statistical stationarity, and based on this, the wall heat fluxes are also averaged over time from $t = 300$ onwards.

The overall effect of increasing pressure ratio is shown in Fig. 15, comparing span-time averaged wall heat fluxes among various cases plotted downstream of the porous layer, from $x = 74$ onwards. It can be noted from the figure that the lowest pressure

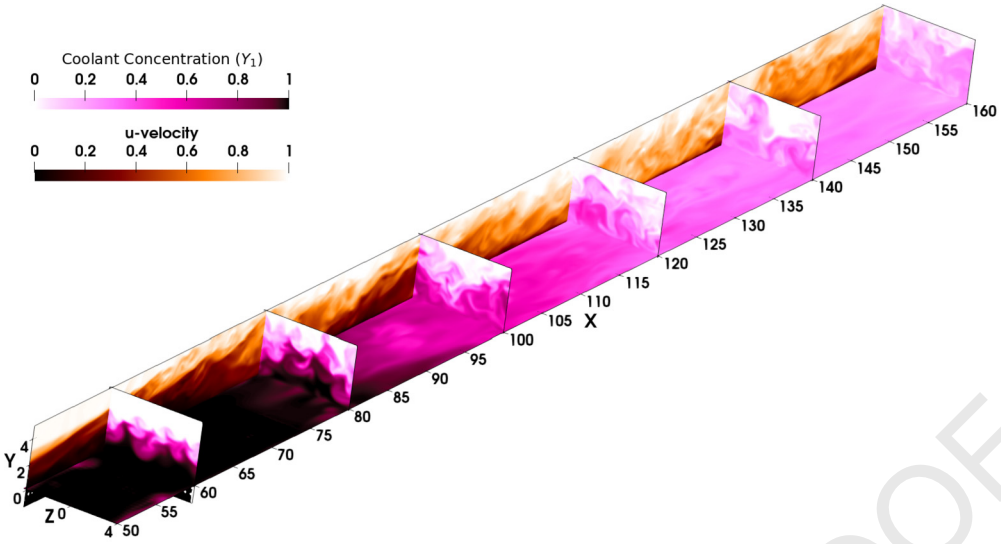

Fig. 10. 3D view of flow field for Case-4a at $t = 462.69$, showing a) coolant concentration (Y_1) on x-z plane at $y = 0.1$ and on various y-z planes along x-direction, b) u-velocity component on x-y plane at $z = -4$.

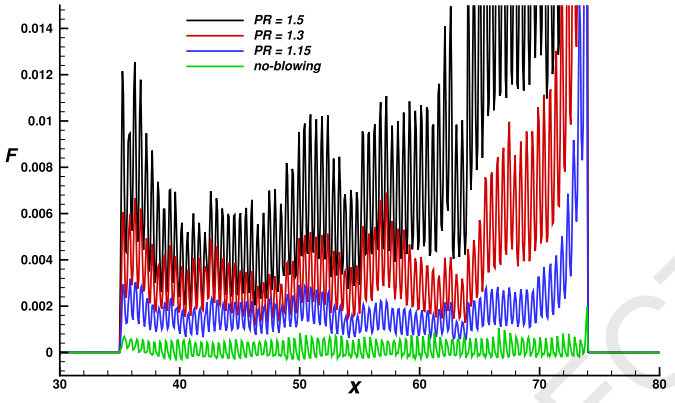

Fig. 11. Span-time averaged values of blowing ratio ($F = \rho v$) for *no-blowing* and various blowing cases at the exit of the porous layer at $y = 0$.

ratio case, Case-2a, with $PR = 1.15$ giving the lowest blowing ratio $F \approx 0.002$, shows the lowest heat flux values downstream of the porous layer up to $x \approx 105$ among all the cases, but then increases to levels slightly above the no-blowing case for $x \geq 105$. The intermediate pressure ratio case, Case-3a, with $PR = 1.3$ giving a blowing ratio $F \approx 0.003$, shows the highest value in the vicinity of the porous layer among all three blowing cases and is also higher than the no-blowing case between $90 \leq x \leq 130$, and eventually matches the wall heat flux values of the *no-blowing* case for $x \geq 130$, showing the worst overall performance among all three blowing cases. The heat fluxes for Case-4a, with $PR = 1.5$ giving a blowing ratio $F \approx 0.065$, show slightly higher values than Case-2a downstream of the porous layer up to $x \approx 105$, but afterwards, show the lowest values of heat fluxes for $x \geq 105$ among all the cases. This can also be noted from the corresponding plots in the bottom frame of Fig. 15 for effectiveness, which is defined as $\eta = (1 - q_{w,c}/q_{w,nc})$, where $q_{w,c}$ and $q_{w,nc}$ are the wall heat fluxes with and without coolant, respectively. It can be seen from the effectiveness plot that $PR = 1.5$ gives the best cooling effectiveness over a longer stretch of flat plate downstream of the porous layer, while Case-2a gives the best performance up to $x \approx 105$, but then worsens. Here also, Case-3a results in the overall worst performance among all the blowing cases.

To further investigate the observed wall heat flux and effectiveness behaviour, Fig. 16 shows the coolant concentration on an x-y plane at $z = -0.001$ for the three PR cases. It can be seen that Case-2a in the bottom frame shows a much smoother coolant film over and downstream of the porous layer trailing edge up to $x \approx 100$. However, for both Case-3a and Case-4a, the coolant flow is already transitional over the porous layer, and hence a more chaotic coolant distribution is noted for these two cases, with mixing starting to occur over the porous layer itself. Further, it can be noted that the highest PR case, Case-4a, leads to the highest mixing of the coolant within the boundary layer. Higher cooling is noted for Case-4a than Case-3a, starting from the trailing edge of the porous layer at $x = 74$. Case-4a also shows the lowest heat flux values after $x \approx 110$ among all the presented cases. For the intermediate case of $PR = 1.3$, although the mixing does start early over the porous layer, the coolant content is far less ($F \approx 0.0030$) compared to the $F \approx 0.0065$ of Case-4a, and hence very high heat flux values are noted for Case-3a, even worse than the *no-blowing* Case-1a. For the lowest PR case, Case-2a, the coolant forms a film immediately downstream of the porous layer up to $x \approx 100$ and then starts to transition, resulting in very high heat fluxes beyond $x \approx 105$ even higher than the *no-blowing* case, Case-1a, and also showing worse performance than the blowing case, Case-3a, farther downstream beyond $x \approx 130$. This point is further illustrated using Fig. 17, which shows the coolant concentration for the three blowing cases at the same y-z plane at $x = 120$. The leftmost frame shows the distribution of coolant for Case-4a, showing the largest content of coolant close to the wall, and also spreads to a higher extent in the wall-normal direction.

4.3. Effect of transition location

As noted previously (see Table 2), the transition point is strongly dependent on the amplitude of the disturbance and more weakly dependent on the streamwise location of the porous surface. In this section, we report another series of runs carried out for the highest observed heat fluxes ($A = 10\%$, $Re_{inj,2}$). This series is denoted as the 'b' series, with details given in Table 4. Fig. 18 compares cases 1a and 1b, i.e., the *no-blowing* cases with the lowest and highest heat transfer from Table 2, showing contours of the u-component of velocity on an x-y plane at $z = -0.001$. The values of u are cut-off at 0.99 to help demarcate the edge of the boundary layer. The boundary layer is seen to be transitioning after the porous sample around $x = 100$ for Case-1a (top frame), while

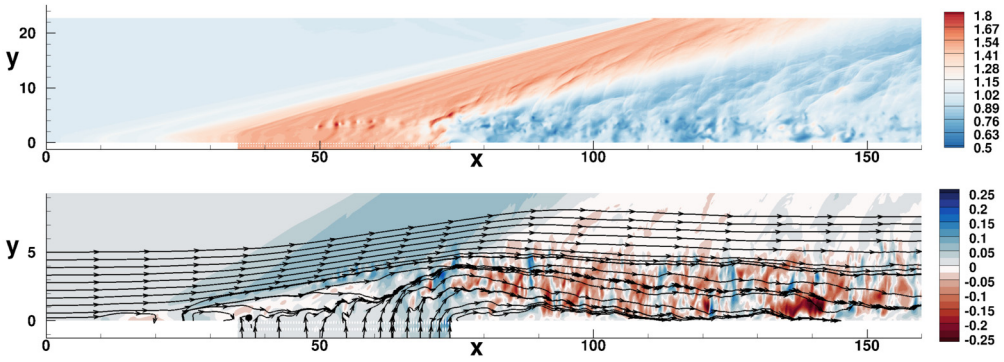

Fig. 12. Non-dimensional pressure contours further scaled with non-dimensional free-stream pressure ($p_\infty = 1/(\gamma M_\infty^2) = 0.02857$) (top frame) and streamtraces with contours of v-component of velocity (bottom frame, stretched in y-direction) on x-y plane at $z = -0.001$ for Case-4a at $t \approx 462$.

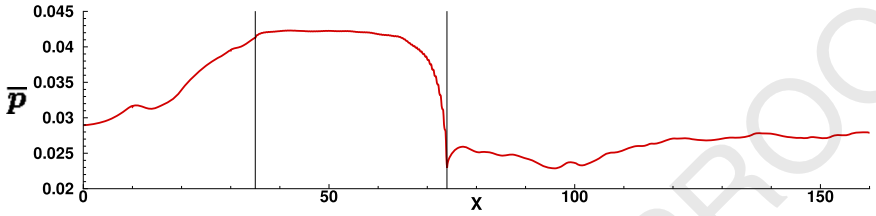

Fig. 13. Span-time averaged pressure ($\overline{p}$) is plotted at the wall for Case-4a.

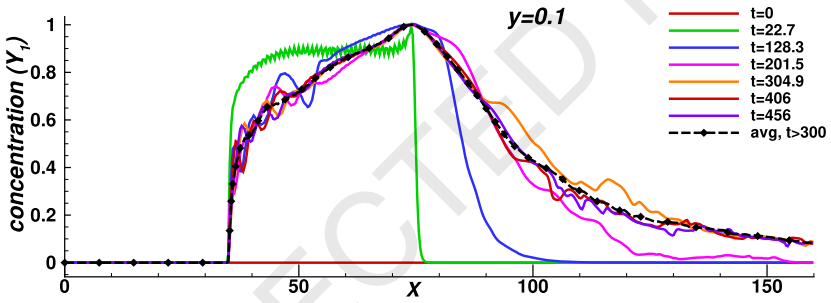

Fig. 14. Time evolution and time-averaged coolant concentration (Y_1) are shown for Case-2a, extracted from x-y plane ($z = -0.001$) along the line at $y = 0.1$ for different times.

Table 4
Cases considered for $Re_{inj,2} = 2.18 \times 10^6$.

Case No.	PR	Disturbance Amplitude
1b	1	10%
2b	1.15	10%
3b	1.3	10%
4b	1.4	10%

for Case-1b, the boundary layer is transitional over the porous sample itself.

To show the transitional nature of the boundary layer, and also to justify the use of the existing grid, the variation of Δy^+ is shown as a function of streamwise distance plotted downstream of the porous layer for the *no-blowing* cases in Fig. 19. The top and bottom frames show variations for $Re_{inj,1}$ and $Re_{inj,2}$, respectively. Since in the existing simulations the cell length in the wall-normal direction is $\Delta y = 24/300 = 0.08$ on level one mesh and $\Delta y = (24/300)/2 = 0.04$ on the second level mesh with a refinement factor of two close to the wall, the first cell centre is located at $y = \Delta y/2 = 0.02$ (or 20×10^{-6} m) from the wall. Therefore, Δy^+ is evaluated at the first cell centre away from the wall, and its value varies from approximately 0.5 to 1 for $Re_{inj,1}$ where the transition is noted to occur downstream of the porous layer around $x \approx 100$ onwards as noted from the increase in the value of Δy^+ from the figure. However, as $Re_{inj,2}$ case is already transitional over the porous layer itself, the Δy^+ starts with a slightly higher value than 1 just downstream of the porous layer and then approaches 1 towards the outflow boundary. These values of Δy^+ result in an adequate resolution of the viscous sub-layer. The cell lengths in x and z-directions on the second level mesh close to the wall are $\Delta x = (160/2000)/2 = 0.04$ and $\Delta z = (8/100)/2 = 0.04$; this implies the maximum values of Δx^+, Δz^+ are twice of that in the y-direction for Δy^+, i.e., approximately 2, i.e., the requirement to resolve the porous layer leads to an over-resolution of the downstream boundary layer. Altogether, these values of Δx^+, Δy^+, and Δz^+ demonstrate that the grid is sufficiently resolved in the present simulations to capture boundary layer properties and wall heat fluxes.

A comparison of time-averaged velocity profiles at $x = 120$ at mid-span are also shown in Fig. 20 for $Re_{inj,1}$ (black line) and $Re_{inj,2}$ (red line) as a function of y. This also demonstrates that for $Re_{inj,2}$, the flow transition begins over the porous sample itself, and hence its profile looks fuller close to the wall and shows a higher gradient of u with y as compared to $Re_{inj,1}$, which only begins to show signs of transition at $x = 120$, as also noted from Fig. 18.

Span- and time-averaged scaled vertical coolant mass flux (i.e., blowing ratio, F) for the various cases from Table 4 is presented in

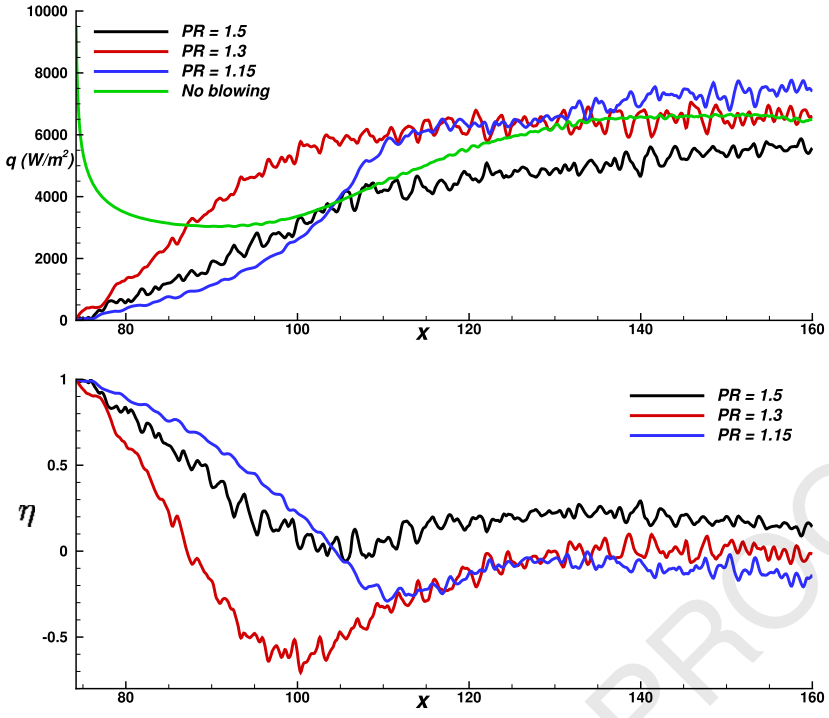

Fig. 15. Wall heat flux values for different cases in the top frame and cooling efficiencies in the bottom frame, plotted downstream of the porous layer from $x = 74$ onwards.

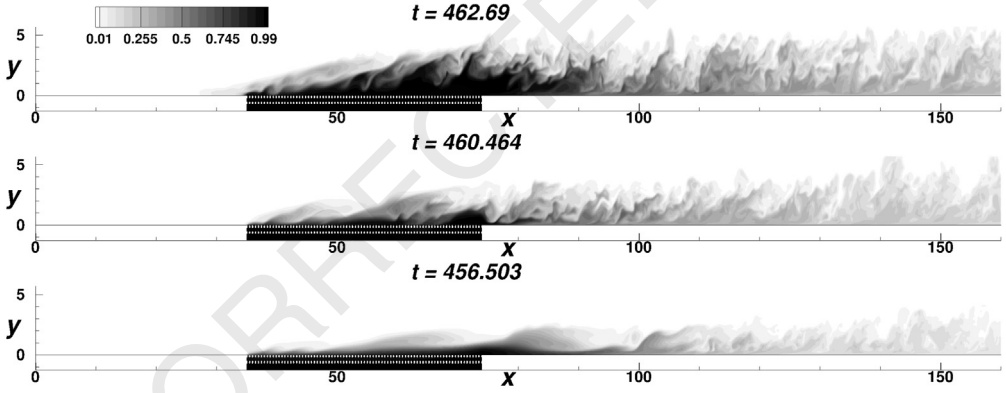

Fig. 16. Coolant concentration (Y_1) shown for the three blowing cases at exact same x-y plane at $z = -0.001$. Top, middle, and bottom frames show Case-4a, Case-3a, and Case-2a, respectively.

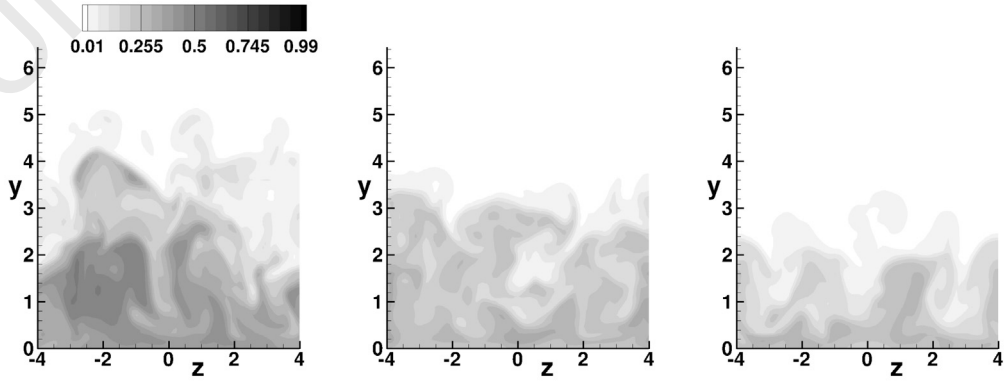

Fig. 17. Coolant concentration (Y_1) shown for the three blowing cases at exact same y-z plane at $x = 120$. The left, middle, and Right frames show Case-4a, Case-3a, and Case-2a, respectively.

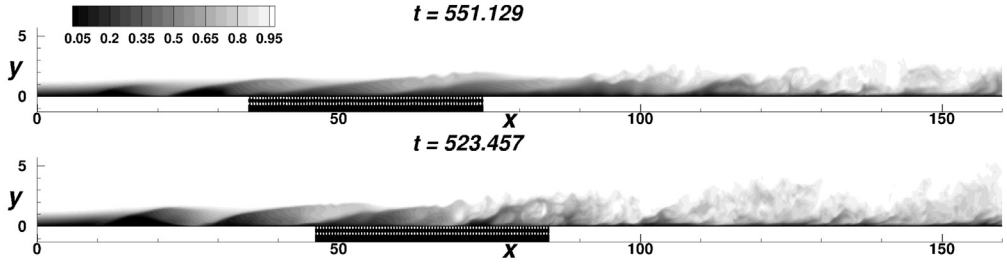

Fig. 18. u-component of velocity at an x-y plane at $z = -0.001$ for no-blowing cases, i.e., Case-1a for $Re_{inj,1}$ (top frame) and Case-1b for $Re_{inj,2}$ (bottom frame).

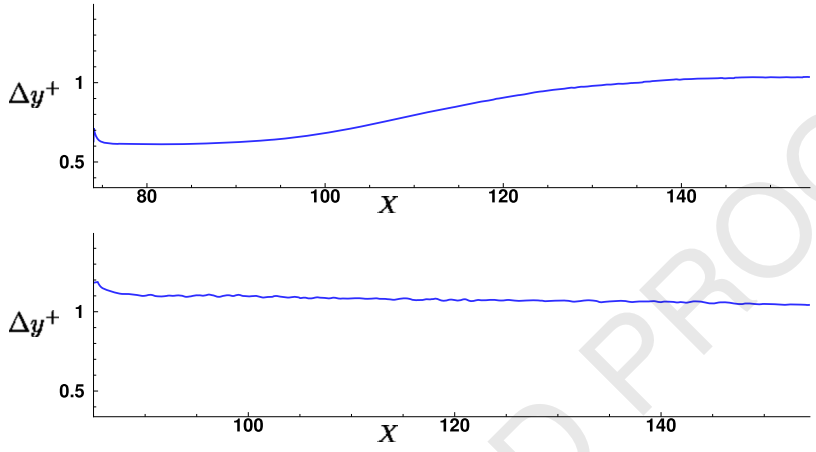

Fig. 19. Streamwise variation of Δy^+ for no-blowing cases, i.e., Case-1a for $Re_{inj,1}$ (top frame) and Case-1b for $Re_{inj,2}$ (bottom frame).

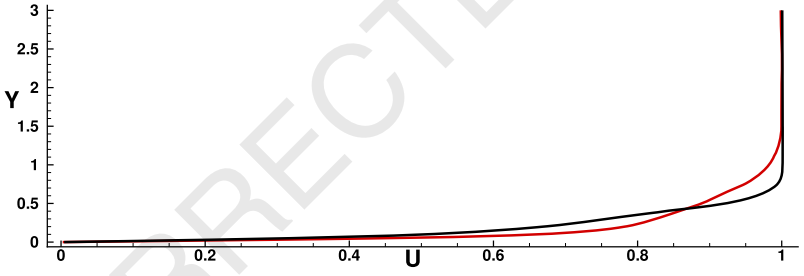

Fig. 20. Time-averaged u-component of velocity at $x = 120$ at mid-span for no-blowing cases, i.e., Case-1a for $Re_{inj,1}$ (black line) and Case-1b for $Re_{inj,2}$ (red line).

Fig. 21 for Case-1b, Case-2b, Case-3b, and Case-4b. A similar pattern in the variation of blowing ratio is noted, as explained earlier in detail for the $Re_{inj,1}$ cases. The velocities dip slightly next to the porous layer leading edge, and there is a large increase towards the trailing edge for the same reasons presented previously. There are also clearly strong variations along the porous surface due to the transition process.

In the top frame of Fig. 22, the wall heat flux variations downstream of the trailing edge of the porous layer, i.e., $x \geq 85$ are plotted for all the cases from Table 4. Here, in general, the wall heat flux values are very high just downstream of the porous layer, as the location of the trailing edge of the porous layer is at $x = 85$, resulting in very-high turbulence levels compared to the $Re_{inj,1}$ cases. Also, the values decrease nearly monotonically with increasing pressure ratios as one moves downstream, compared to the unusual variations seen in the case of $Re_{inj,1}$. The wall heat flux values are substantially higher for the *no-blowing* case than the blowing cases, suggesting that the coolant addition is effectively reducing the wall heat fluxes. A slight decrease compared to the no-blowing case is seen for Case-2b, which is the least pressure/blowing ratio case. However, a significant drop in heat flux values is noted for Case-3b and Case-4b, where significantly higher blowing ratios are observed. Case-4b shows lowest values of heat fluxes just downstream of the trailing edge, however the values become comparable with Case-3b as one moves further downstream.

The cooling effectivenesses are also shown in the bottom frame of Fig. 22. It can be clearly seen that among all the blowing cases, Case-4b gives the highest effectiveness, with Case-3b following it closely. However, Case-2b shows the lowest effectiveness among the blowing cases.

To explain these observed wall heat flux variations, Fig. 23 shows coolant concentration contours for the three blowing cases. It can be noted that for this slightly higher injection Reynolds number $Re_{inj,2} = 2.18 \times 10^6$, the boundary layer is already transitional over the porous layer itself, even for the case of lowest blowing ratio, Case-2b. However, because Case-2b has the lowest blowing ratio and hence the lowest coolant content, it is seen to perform marginally better than the *no-blowing* case, Case-1b. As the blowing ratios for Case-3b and Case-4b are much higher and somewhat similar, the wall heat fluxes and the cooling effectiveness in both cases are similar, giving the highest cooling performance among all the cases. The higher amplitude of disturbances

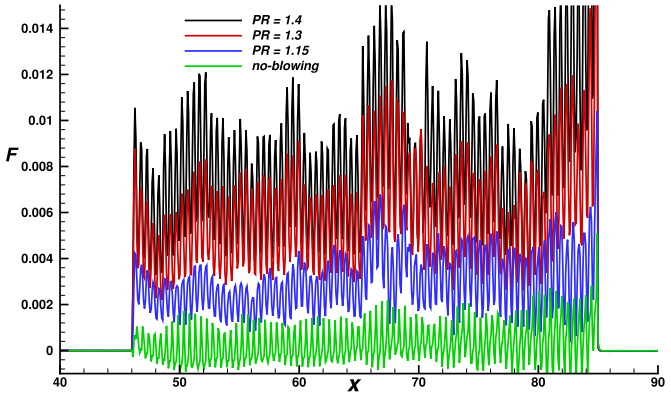

Fig. 21. Span-time averaged values of blowing ratio ($F = \rho v$) at the exit of the porous layer at $y = 0$.

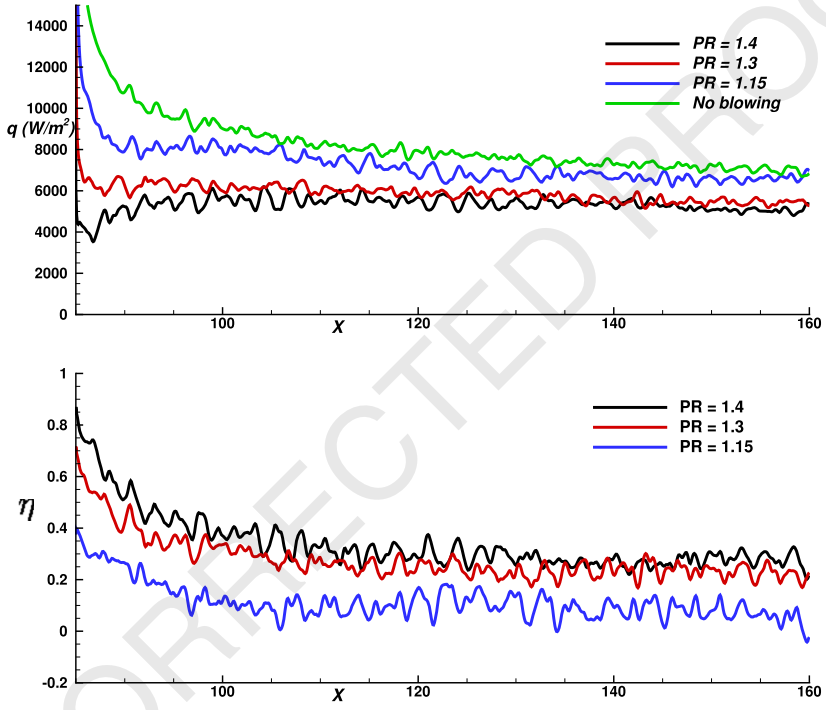

Fig. 22. Wall heat flux values for different cases in the top frame and cooling efficiencies in the bottom frame, plotted downstream of the porous layer from $x = 85$ onwards.

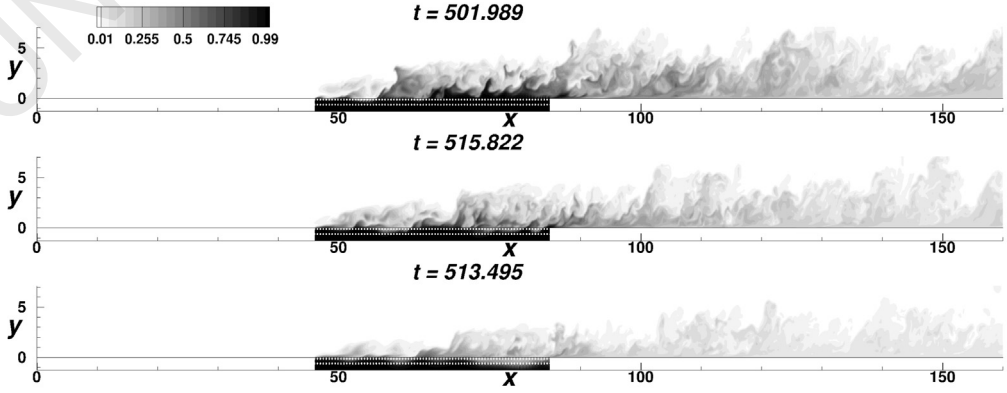

Fig. 23. Coolant concentration (Y_1) shown for the three blowing cases at exact same x-y plane at $z = -0.001$. The top, middle, and bottom frames show Case 4b, Case 3b, and Case 2b, respectively.

for the higher $Re_{inj,2}$ cases introduce more vigorous mixing of the coolant, and hence, the trend of lower wall heat fluxes is generally observed in all the blowing cases compared to the *no-blowing* case, Case-1b.

5. Conclusions

In the present study, the transpiration cooling technique is explored at Mach number $M_\infty = 5$ to mitigate the high wall heat flux loads experienced in very high speed regimes. Various cases, with and without coolant blowing, are simulated, presenting an overall picture of the flow conditions. Transition plays a critical role in terms of the observed wall heat fluxes and flow perturbations are seen to penetrate within the porous sample. In all the cases, the blowing distribution is non-uniform, with depressed blowing ratios due to the pressure rise across the oblique shock that is caused by the injection, and an expansion fan at the trailing edge of the porous surface that increases the local blowing towards the rear of the sample.

For cases where flow transition occurs downstream of the sample when no coolant is blown, the cooling is far more effective immediately downstream of the porous sample for the lowest blowing ratio case due to the film formation. However, once transition is triggered downstream, the effectiveness quickly worsens. The intermediate blowing ratio case performs worst as it triggers the transition over the sample itself while the coolant concentration is still low. A significantly higher blowing ratio case, however, shows better performance for a longer stretch downstream of the porous sample, despite the transition happening over the porous sample. For the cases where transition occurs over the porous sample itself when no coolant is blown, the results are more consistent. The cooling effectiveness increases with increasing blowing ratios, showing best performance for the highest blowing ratio case.

Therefore, the study elucidates the importance of flow transition on the cooling performance for a single porous sample placed in a flow at a high unit Reynolds number and Mach $M_\infty = 5$ at different injection locations of the porous layer and different blowing ratios. This study is also a culmination of the efforts started in [10] and [15], and presents a detailed analysis of the mesoscopic sphere model proposed in [15] in the context of experimentally observed hypersonic boundary layer flows, where transpiration cooling is achieved using the coolant injection through actual porous ceramics materials.

It is also important to note some of the limitations of the present study, e.g., the use of sphere model with high porosity to make it tractable for direct numerical simulation, which otherwise becomes very expensive with very small grid spacings and time step requirements. Additionally, slightly higher levels of perturbations were used in a smaller computational domain with an inflow far downstream of the flat plate leading edge to mimic the behaviour seen in the experiments, where the setup has a sharp leading edge and a longer stretch for the instabilities to grow till they reach the porous layer. Also, only three layers of spheres are used for the thickness of the porous layer. Considering these limitations, simulations for a flat plate with a leading edge along with a porous layer with less porosity and more sphere layers could be performed in the future.

Declaration of competing interest

The authors declare that they have no known competing financial interests or personal relationships that could have appeared to influence the work reported in this paper.

Data availability

Data will be made available on request.

Acknowledgements

The authors would like to acknowledge support from EPSRC (Engineering and Physical Sciences Research Council) under Grant No. EP/P000878/1. The authors also acknowledge the use of the IRIDIS High Performance Computing Facility, and associated support services at the University of Southampton, to accomplish this work.

References

[1] O. Uyanna, H. Najafi, Thermal protection systems for space vehicles: a review on technology development, current challenges and future prospects, Acta Astronaut. 176 (2) (2020) 341–356.
[2] Z. Min, G. Huang, S.N. Parbat, L. Yang, M.K. Chyu, Experimental investigation on additively manufactured transpiration and film cooling structures, J. Turbomach. 141 (3) (2019).
[3] T. Furumoto, A. Koizumi, M.R. Alkahari, R. Anayama, A. Hosokawa, R. Tanaka, T. Ueda, Permeability and strength of a porous metal structure fabricated by additive manufacturing, J. Mater. Process. Technol. 219 (2015) 10–16.
[4] E. David, Glass, ceramic matrix composite (CMC) thermal protection systems (TPS) and hot structures for hypersonic vehicles, Tech. Rep. AIAA-2008-2682, NASA Langley Research Center, Hampton, Virginia 23681, 2008.
[5] R.J. Goldstein, E.R.G. Eckert, F.K. Tsou, A. Haji-Sheikh, Film cooling with air and helium injection through a rearward-facing slot into a supersonic air flow, AIAA J. 4 (6) (1966) 981–985.
[6] A.D. Fitt, J.R. Ockendon, T.V. Jones, Aerodynamics of slot-film cooling: theory and experiment, J. Fluid Mech. 160 (1985) 15–27.
[7] A.D. Fitt, P. Wilmott, Slot film cooling-the effect of separation angle, Acta Mech. 103 (1–4) (1994) 79–88.
[8] S. Wittig, A. Schulz, M. Gritsch, K.A. Thole, Transonic film-cooling investigations: effects of hole shapes and orientations, in: Turbo Expo: Power for Land, Sea, and Air, ASME, 1996, V004T09A026.
[9] Z. Yinhai, P. Wei, X. Ruina, P. Jiang, Review on active thermal protection and its heat transfer for airbreathing hypersonic vehicles, Chin. J. Aeronaut. 31 (10) (2018) 1929–1953.
[10] A. Cerminara, T. Hermann, H.S. Ifti, R. Deiterding, N. Sandham, M. McGilvray, Influence of instability modes on cooling performance in hypersonic boundary layer with slot injection, Aerosol Sci. Technol. 109 (2021) 106409.
[11] M. McGilvray, L.J. Doherty, A.J. Neely, R. Pearce, P. Ireland, The Oxford high density tunnel, in: 20th AIAA International Space Planes and Hypersonic Systems and Technologies Conference, AIAA 2015-3548, 2015.
[12] T. Langener, J.V. Wolfersdorf, J. Steelant, Experimental investigations on transpiration cooling for scramjet applications using different coolants, AIAA J. 49 (7) (2011) 1409–1419.
[13] J. Meinert, J. Huhn, E. Serbest, O.J. Haidn, Turbulent boundary layers with foreign gas transpiration, J. Spacecr. Rockets 38 (2) (2001) 191–198.
[14] T. Hermann, H.S. Ifti, M. McGilvray, L. Doherty, R.P. Geraets, Mixing characteristics in a hypersonic flow around a transpiration cooled flat plate model, in: HiSST: International Conference on High-Speed Vehicle Science and Technology, Moscow, Russia, 2018.
[15] A. Cerminara, R. Deiterding, N. Sandham, A mesoscopic modelling approach for direct numerical simulations of transition to turbulence in hypersonic flow with transpiration cooling, Int. J. Heat Fluid Flow 86 (2020) 108732.
[16] K.A. Heufer, H. Olivier, Experimental and numerical study of cooling gas injection in laminar supersonic flow, AIAA J. 46 (11) (2008) 2741–2751.
[17] M.A. Keller, M.J. Kloker, H. Olivier, Influence of cooling-gas properties on film-cooling effectiveness in supersonic flow, J. Spacecr. Rockets 52 (5) (2015) 1443–1455.
[18] M.A. Keller, M.J. Kloker, Direct numerical simulation of foreign-gas film cooling in supersonic boundary-layer flow, AIAA J. 55 (1) (2016) 99–111.
[19] A. Gülhan, S. Braun, An experimental study on the efficiency of transpiration cooling in laminar and turbulent hypersonic flows, Exp. Fluids 50 (3) (2011) 509–525.
[20] N. Christopher, J.M. Peter, M.J. Kloker, J.-P. Hickey, DNS of turbulent flat-plate flow with transpiration cooling, Int. J. Heat Mass Transf. 157 (2020) 119972.
[21] W. Dahmen, S. Müller, M. Rom, S. Schweikert, M. Selzer, J. Von Wolfersdorf, Numerical boundary layer investigations of transpiration-cooled turbulent channel flow, Int. J. Heat Mass Transf. 86 (2015) 90–100.
[22] R. Ding, J. Wang, F. He, G. Dong, L. Tang, Numerical investigation on the performances of porous matrix with transpiration and film cooling, Appl. Therm. Eng. 146 (2019) 422–431.
[23] J. Anderson, Hypersonic and High-Temperature Gas Dynamics, AIAA Education Series, AIAA, Inc., 2019.
[24] P.D. Neufeld, A.R. Janzen, R.A. Aziz, Empirical equations to calculate 16 of the transport collision integrals $\Omega^{(l,s)*}$ for the Lennard-Jones (12–6) potential, J. Chem. Phys. 57 (3) (1972) 1100–1102.

[25] R. Deiterding, Construction and application of an amr algorithm for distributed memory computers, in: Adaptive Mesh Refinement-Theory and Applications, Springer, 2005, pp. 361–372.
[26] D.J. Hill, D.I. Pullin, Hybrid tuned center-difference-WENO method for large eddy simulations in the presence of strong shocks, J. Comput. Phys. 194 (2) (2004) 435–450.
[27] C. Pantano, R. Deiterding, D.J. Hill, D.I. Pullin, A low numerical dissipation patch-based adaptive mesh refinement method for large-eddy simulation of compressible flows, J. Comput. Phys. 221 (1) (2007) 63–87.
[28] J.L. Ziegler, R. Deiterding, J.E. Shepherd, D.I. Pullin, An adaptive high-order hybrid scheme for compressive, viscous flows with detailed chemistry, J. Comput. Phys. 230 (20) (2011) 7598–7630.
[29] M. Ihme, Y. Sun, R. Deiterding, Detailed simulations of weak-to-strong ignition of a $H_2/O_2/Ar$ mixture in shock-tubes, in: International Symposium on Shock Waves, Springer, 2013, pp. 209–214.
[30] R. Deiterding, Block-structured adaptive mesh refinement-theory, implementation and application, in: Esaim: Proceedings, vol. 34, EDP Sciences, 2011, pp. 97–150.
[31] S. Lee, J. Yang, Modeling of Darcy-Forchheimer drag for fluid flow across a bank of circular cylinders, Int. J. Heat Mass Transf. 40 (13) (1997) 3149–3155.
[32] S. Ergun, A.A. Orning, Fluid flow through randomly packed columns and fluidized beds, Ind. Eng. Chem. 41 (6) (1949) 1179–1184.